npj computational materials

www.nature.com/npjcompumats

ARTICLE OPEN

Check for updates

# Computational screening of transition metal-doped CdS for photocatalytic hydrogen production

Yuting Li[1,2], Daniel Bahamon[1,2], Mutasem Sinnokrot[1,3] and Lourdes F. Vega[1,2]✉

A novel computational screening study of single transition metal (TM), TM-doped, and dual TMs-doped on CdS (110) surfaces via DFT calculations is presented, focusing on their stability and catalytic activity, searching for efficient photocatalysts for hydrogen production. Criteria based on key performance descriptors allowed to fine-tune the selection. Results indicate that TM dopants can reduce the energy band gap and enhance impurity d-states. Pt, Rh, and Pd were found to be the best dopants in TM-doped CdS, since their $|\Delta G_H|$ is 80% smaller compared to the pristine CdS surface. Moreover, TM1-TM2-co-doped CdS catalysts show better performance for the hydrogen evolution reaction (HER) due to synergistic effects of the two TMs, where Co-Pt, Pd-Pt and Co-Rh co-doping CdS significantly reduced $|\Delta G_H|$ to less than 0.1 eV. Results point out four promising novel co-catalysts (i.e., Co, Co-Pt, Co-Rh, Rh-Ag) with very good performance in HER, to be further explored in experimental studies.

*npj Computational Materials* (2022)8:229 ; https://doi.org/10.1038/s41524-022-00922-4

## INTRODUCTION

The impact of greenhouse gases emitted from the consumption of fossil fuels on climate change renders green hydrogen an ideal and sustainable energy source for the near future. This green hydrogen can be produced, among other methods, from water and/or hydrogen sulfide photocatalysis utilizing solar energy without any greenhouse gas emissions[1–4]. As a consequence, the semiconductors utilized in $H_2O$ and $H_2S$ photocatalysis have attained considerable scientific attention for their potential to use solar energy for the hydrogen evolution reaction (HER)[5–10].

Cadmium sulphide (CdS) has been extensively studied as a visible light-active semiconductor for HER by virtue of its low cost, proper band edges for visible light response, and proton reduction[11,12]. However, the facile recombination of electron-hole pairs and the poor photo-stability of bare CdS make its wide application in various photocatalysis fields very challenging. Loading co-catalysts[11,13] on the catalyst surface has proved to be an efficient approach to regulate the electronic structures and enhance the photocatalytic activity of materials for various applications. Particularly, experimental work has been done on doping CdS catalysts with transition metals (TM), such as Pt[14–24], Pd[20–22], Rh[20–22], Ru[20,22], Cu[25], Ni[26], co-doped Pt-Pd[27], co-doped Zn-Cu[28], and co-doped Ti-Ni[29], among others. These experimental works determined that suitable co-catalysts could provide trapping sites for the photogenerated electrons, improve the stability of the catalysts by timely consuming the photogenerated charges, and provide active sites for the HER, significantly reducing the reaction barriers and achieving high photocatalytic efficiency[30]. However, despite these advances, achieving higher quantum yields and selectivity still poses a great challenge, making it essential to understand how to improve visible light utilization and conversion efficiency.

In recent years, advances in DFT calculations have proven to be very helpful in guiding the selection or design of catalysts for efficient hydrogen generation, significantly accelerating the development of new catalysts[31–34]. For instance, Zhou et al.[35] investigated various adsorption geometries of H*, HO*, O*, and H*/HO* on CdS and ZnS (110) surfaces, and explained the experimental fact that bare CdS is not an active photocatalyst for water splitting, but that Pt co-catalyst could significantly improve the catalytic activity and HER efficiency. Garg et al.[36] studied the electrocatalytic activity of TM -doped CdS nanotubes (TM = Fe, Co, Ni, Cu, Ru, Rh, Pd, Ag, Os, Ir, Pt, and Au) for electrochemical water splitting by spin-polarized DFT calculations. Activity analysis indicated that Pd- and Ru-doped CdS with the lowest overpotential were the best catalysts for oxygen evolution reactions and HERs, respectively, outperforming pristine CdS nanotubes and bulk CdS. Wu et al.[37] used DFT to investigate the formation and electronic structures of native defects and TM (Mn, Fe, Co, and Ni) doping on zinc-blended CdS. Ni doping significantly narrowed the band gap of zinc-blended CdS, which indicated that proper loading of Ni improved the light adsorption performance of nano-sized CdS photocatalysts. Moreover, co-doping of active metals would further enhance the catalytic activity over single-doped catalysts. In this regard, Kim et al.[38] investigated 13 dopant TMs (Mn, Fe, Co, Ni, Cu, Ru, Rh, Pd, Ag, Os, Ir, Pt, Au) and their 91 binary combinations for co-doping into $CeO_2$ surfaces. They found that Cu and (Cu, Ag) with the lowest oxygen vacancy formation energy were the optimal candidates among the single and binary dopants, respectively.

To the best of our knowledge, previous studies have almost exclusively focused on the applications of electrocatalysis and the doping effects on the catalysts' fundamental properties. Therefore, systematic theoretical analysis is still required for developing multifunctional, highly active, and stable catalysts for photo-induced $H_2O$ and $H_2S$ splitting, especially working on the dual metal co-catalyst. Hence, a top-down approach is used to perform a systematic computational screening to identify the proper co-catalysts that meet the desired requirements for photocatalytic $H_2O$ and $H_2S$ splitting. Inspired by previous catalyst screening studies[39,40], we have investigated TMs from 3d (Sc, Ti, V, Cr, Mn, Fe, Co, Ni, and Cu), 4d (Ru, Rh, Pd, and Ag), and 5d (Os, Ir, Pt, and Au) series doped at the Cd vacancy site of the CdS (110) surface. Selected dual transition metals co-doped into the CdS (110) surface were also investigated by DFT calculations, to assess their performance *vs*. single metal dopants.

[1]Research and Innovation Center on CO2 and Hydrogen (RICH), Khalifa University, PO Box 127788, Abu Dhabi, UAE. [2]Chemical Engineering Department. Khalifa University, PO Box 127788, Abu Dhabi, UAE. [3]Chemistry Department, Khalifa University, PO Box 127788, Abu Dhabi, UAE. ✉email: lourdes.vega@ku.ac.ae

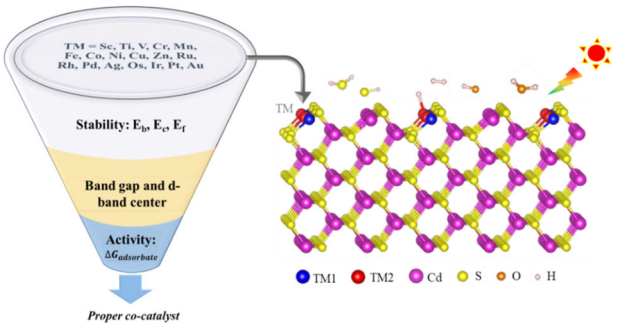


**Fig. 1 Screening protocol for the discovery of transition metal-doped CdS catalysts.** The followed process includes (1) examination of the structural stability ofdifferent TM@CdS surfaces based on their corresponding binding energies ($E_b$), cohesive energies ($E_c$), and formation energies ($E_f$); (2) the band gap and d-band center to estimate the optical and electronic properties; (3) the change in the Gibbs free energy (ΔG) of the adsorbates. The right panel shows a schematic representation of theTM-doped CdS (110) catalyst.

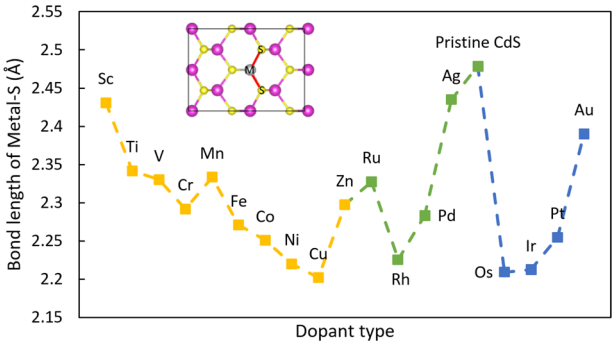


**Fig. 2 Bond length between the doped metal and sulfur atoms on the top layer of TM@CdS surfaces.** The order of the TM dopant from left to right is as follows: 3d series (yellow), 4d series (green), and 5d series (blue). The dashed line is a guide to the eyes.

## RESULTS AND DISCUSSION

Figure 1 shows a schematic diagram of the followed screening process for determining the proper TMs doped on the CdS (110) surface in terms of selected descriptors for green hydrogen generation; details about the screening workflow are provided in the METHODS section. We first investigated selected properties of single TM-doped on the surface ($Cd_{1-x}TM_xS, x = 0.035$, hereinafter referred as TM@CdS), followed by searching for the presence of synergistic effects on the catalyst stability and activity of dual metal-doped CdS system ($Cd_{1-x-y}TM_xTM_yS, x + y = 0.07$, denoted as TM-TM@CdS). Finally, the TMs and binary TM dopants fulfilling the screening criteria were determined as the most suitable photocatalysts for HER.

### Structural features and stabilities of the TM@CdS

Optimized geometric features of TM@CdS surfaces (depicted in Supplementary Fig. 1) show that a single TM-doped on the surface does not drastically change the orientation of the crystal lattice, and the TM@CdS surface remains highly symmetric. However, TM doping induces the change of adjacent atom positions and deformations of local bond lengths to reach a new equilibrium state. The bond length values between metal and sulfur atoms on the first layer of TM@CdS surfaces are presented in Fig. 2. It should be mentioned that the bond length of Cd-S in the pristine CdS (110) surface was found to be 2.48 Å, consistent with previous DFT calculations[35]. After embedding one TM atom on the top layer of the defective CdS surface, the metal–sulfur bond length was reduced by up to 11%, where Cu@CdS surface contains the shortest metal–sulfur distance. Comparing the results in the same series, the overall trend of bond length in 3d series decreases with the increasing of the atomic number; however, the reverse trend is observed for the late transition metals in 4d and 5d series, and there are specific discontinuities for Mn and Ru dopants. In order to interpret the bond length variation, we further explored the spin magnetization, oxidation states and partial charge density of the TMs (included in Supplementary Table 1). According to the spin analysis, it was found that the oxidation states of the TM dopant atoms were the same as the Cd(II) site, although, the spin magnetization and partial charge density are different between all TMs. We also found that the pattern of bond length is consistent with the pattern of partial charge density variation. This observation can be attributed to the variations in the ionic radius of TM, explicit charge transfer between the TM and the ligand, and their valence electrons in the (*n-1*)d and *ns* orbitals.

As structural and chemical stability are universally applied metrics to evaluate a dopant as a reliable co-catalyst, the structural stability of the TM@CdS surfaces was investigated in this work. The binding energies ($E_b$, see Eq. (1)) of transition metal atoms embedded in the CdS surface, and the cohesive energies of bulk metal ($E_c$, see Eq. (2)) are graphically represented in Fig. 3. All calculated $E_b$ of TM@CdS present negative values, with the Sc@CdS being the most negative one (i.e., −8.26 eV) and Ag@CdS being the least negative (i.e., −4.02 eV). These values are similar to those found in previously available computational studies[39,41]. It is noticeable that $E_b$ values exhibit an upward trend from Sc to Zn in 3d TM-doped systems. Likewise, Ru to Ag in 4d series and Os to Au in the 5d series display the same upward trend. These results suggest that the later TM atoms (e.g., Zn, Ag, Au) are less prone to form single active sites on the CdS surface. It is also observed in Fig. 3 that the $E_b$ of all doped specimens are more negative than their corresponding $E_c$, excluding Os@CdS, indicating that the aggregation of TM atoms is unfavorable for most of the studied TM atoms, stably and uniformly doping the CdS surface, and acting as active sites. Thus, the TM@CdS surfaces, except Os@CdS, would present excellent stability in catalytic reactions.

Furthermore, the formation energies ($E_f$, see Eq. (3)) of TM@CdS were calculated, and results are presented in Fig. 3. The $E_f$ of TM@CdS ranges from −0.63 eV (Sc@CdS) to −0.54 eV (Os@CdS). Os@CdS shows the largest $E_f$, pinpointing possible difficulties of experimentally preparing this catalyst. Considering the three types of calculated energies, it is fair to say that most of the TM@CdS, except Os@CdS, can be easily prepared experimentally, potentially having better catalytic performance in the HER than bare CdS. Therefore, Os@CdS system is discarded for the next step of the evaluation.

### Electronic structure of the TM@CdS catalysts

The electronic structure can provide deep insights into how to optimize the efficiency and activity of photocatalysts. As presented in Fig. 4, doping one TM atom on the CdS surface causes a decrease in the band gap by enhanced impurity states near the Fermi level, which is beneficial for electron transfer and photocatalytic reactions. The validation of the predicted band gaps with the pristine CdS and some TM@CdS can be found in Supplementary Table 2, showing very close results, with errors below 5%, thus corroborating the reliability of the calculations.

As inferred from Fig. 4, the top energy potential of the valence band of pristine CdS surface is more positive than the oxidation potential of $S/H_2S$ and $O_2/H_2O$, and the bottom energy potential of the conduction band is more negative than the reduction potential of $H^+/H_2$, indicating that $H_2S$ and $H_2O$ dissociation reactions can be carried out at this pristine CdS surface. Meanwhile, the valence band maximum (VBM) and conduction band minimum (CBM) of all TM@CdS materials are more negative and more positive than the hydrogen reduction potential and the $S^{2-}$ oxidation potential, respectively. However, the band edges of

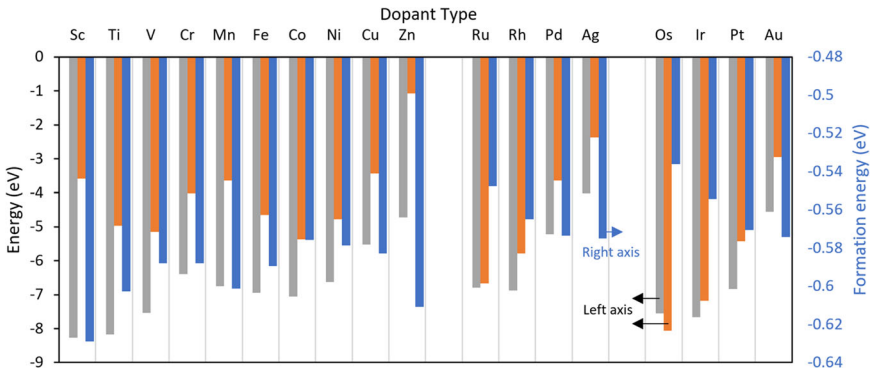


**Fig. 3 Binding energy $E_b$ (gray column, left axis) of TM embedded into CdS catalyst, cohesive energy $E_c$ (orange column, left axis) of TM bulk, and formation energy $E_f$ (blue column, right axis) of TM@CdS catalyst.** The order of the TM dopant from left to right goes from 3d series to 5d series. Data are available in Zenodo.

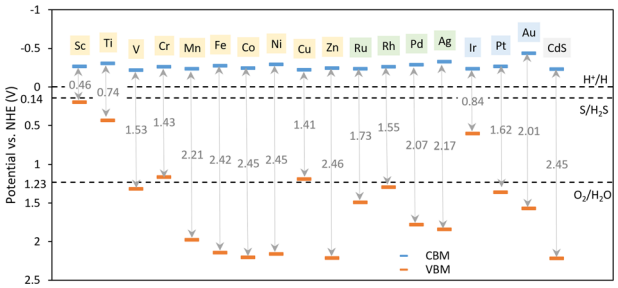


**Fig. 4 Relationship between band structure of TM@CdS semiconductor and redox potentials of $H_2S$ and $H_2O$ decomposition computed with the HSE06 hybrid functional.** The order of the TM dopant from left to right: 3d series (highlighted in yellow), 4d series (highlighted in green), and 5d series (highlighted in blue). Data are available in Zenodo.

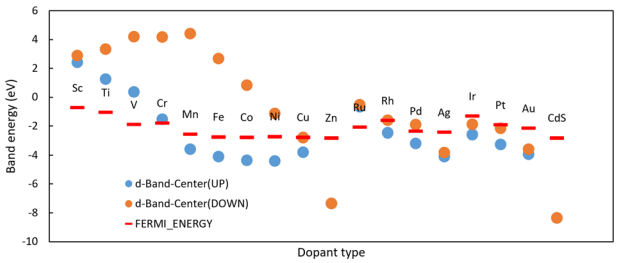


**Fig. 5 Calculated spin-polarized *d*-band centers relative to the Fermi level for TM@CdS structures.** Data are available in Zenodo.

Sc@CdS, Ti@CdS, Cr@CdS, Cu@CdS, and Ir@CdS do not straddle the water oxidation potentials, demonstrating that they can only be utilized for the $H_2S$ splitting process because the driving force for $H_2O$ splitting reaction is not strong enough. Additionally, Sc@CdS, Ti@CdS, and Ir@CdS exhibit a band gap smaller than 1.23 eV, suggesting that Sc, Ti, and Ir are not good potential dopants for photocatalytic $H_2S$ and $H_2O$ splitting.

With respect to the order from 3d to 4d series, the early TM dopants significantly reduce the energy gap and tune the electronic structure of the surface, pointing out that it is much easier to excite an electron from the bound state into a free state, where it can participate in conduction, resulting in a very high reactivity. Miller et al.[42] also demonstrated that early TMs are very reactive with excessively tight binding to the reaction intermediates and thus poisoning the catalyst surface, while the late TMs, especially the metals with high oxidation states ($d^8$, $d^9$ states) provide the most desirable balance in adsorption and desorption behavior. Moreover, pristine CdS suffers severe photocorrosion under light irradiation due to the rapid recombination of the excited electrons and holes, but TM@CdS catalysts have lower reduction potential compared to pristine CdS, as electrons transfer from CdS to TM. Hence, TM dopants could serve as electron reservoirs to trap electrons from the conduction band of CdS, which promotes electron extraction and slows the recombination of electron-hole pairs. It is also observed that TM@CdS surfaces show narrower band gaps compared to pristine CdS, which can increase visible light adsorption capability and, consequently, enhance the photocatalytic HER performance.

The *d*-band center for metals has been extensively utilized to study activity trends in catalytic reactions on metal surfaces[43]. When spin polarization is considered in the calculation for magnetic surfaces, it is desirable to consider two *d*-band centers, i.e., spin-up states and spin-down states; when the degree of the spin polarization is smaller, the two *d*-band centers are close to each other[43]. The converged spin magnetization for the studied TM metals has been included in Supplementary Table 1. Figure 5 presents the energy of the spin-polarized *d*-band center relative to the Fermi level for the studied systems. It was found that the *d*-band centers of different transition metals dopants are in the range of −6.71 to 3.35 eV, being the relative distance between the *d*-band center energy and its Fermi energy for pristine CdS surface, the second largest compared to other systems. In the TM-doped systems, as the *d*-states approaches the Fermi energy, antibonding orbitals can be shifted up through the Fermi level and become an empty molecular orbital to increase the bond strength. Therefore, doping one TM atom to the CdS catalyst surface is beneficial to increase the energy of the *d*-states relative to the Fermi level, modifying the band structure of the bare catalyst and further improving the adsorption strength and catalytic activity. The impurity *d*-states of TMs placed near the Fermi level could also increase the electrical conductivity compared to pristine CdS surface, confirmed by partial DOS analysis in a previous work[36]. Figure 5 also shows that Sc, Cu, Zn, Ru, Rh, Pd, Ag, Ir, Pt, and Au-doped CdS surfaces are non-magnetic, because of the similar *d*-band center locations from spin-up and spin-down states (i.e., the spin-up and down of density of states, DOS, are highly symmetric). Other considered TMs-doped surfaces show significant inconsistent *d*-band center locations, being magnetic; these sub-bands further split into majority (spin-up, blue dots in Fig. 5) and minority (spin down, yellow dots in Fig. 5) spin sub-bands, and only spin minority electrons take part in the bonding with the adsorbate in the ferromagnetic case[44]. As highlighted by Gao et al.[45], "the higher d-electron occupation and deeper d-band center (of spin down) normally result in a weaker intermediate's binding strength". Therefore, based on this relative distance between the *d*-band center energy of the minority spin and the Fermi energy

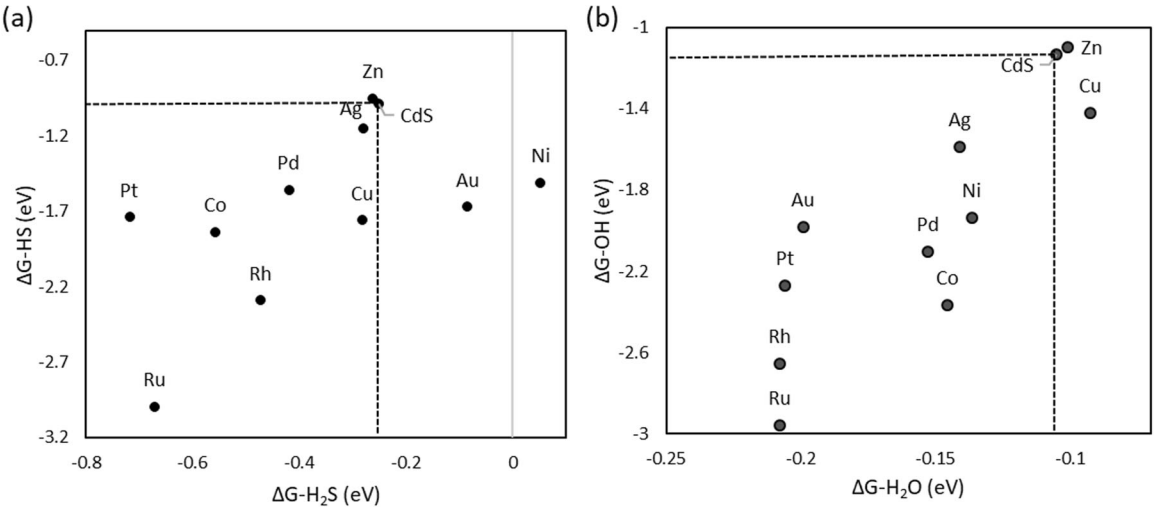


**Fig. 6 Adsorption energies on thepristine CdS (110) surface and TM@CdS surfaces.** Gibbs free energies (ΔG) for $H_2S$ and HS (**a**), and energies for $H_2O$ and OH (**b**). The dashed line was set to compare the results of TM@CdS systems with pristine CdS surface. Data are available in Zenodo.

($|\varepsilon_d - E_f|$), the catalyst activity shows the following order: Cu > Rh > Pt > Pd > Ir > Ag > Au > Ru > Ni > Co > Sc > Ti > Zn > Fe ≈ CdS > Cr > V > Mn. Consequently, TM@CdS catalysts with $|\varepsilon_d - E_f|$ smaller than the pristine CdS surface are considered as a criterion for improved catalytic activity via TM doping. Hence, Fe, Cr, V, and Mn @CdS are excluded from the rest of the analysis performed in this work, based on the *d*-band center calculations, leaving Cu, Rh, Pt, Pd, Ag, Au, Ni, Ru, Co, Zn @ CdS catalysts as the ones to be further investigated for the adsorption of $H_2S$, $H_2O$ and their dissociation intermediates.

### Comparison between $H_2S$ and $H_2O$ splitting on TM@CdS surfaces

For $H_2S$ and $H_2O$ splitting processes, we have considered the important reaction steps relevant to $H_2S$ adsorption, $H_2S$ dissociation, $H_2O$ adsorption, and $H_2O$ dissociation, respectively, and HER steps. The dissociation reactions for $H_2S$ and $H_2O$ are initiated with the splitting of one S–H bond and O–H bond for the subsequent formation of HS and OH on the catalyst's surface, respectively. Therefore, to investigate the dissociation of $H_2S$ and $H_2O$ on the TM@CdS surfaces, the adsorption structures and energies of $H_2S$, HS, $H_2O$, and OH on Co, Ni, Cu, Zn, Ru, Rh, Pd, Ag, Pt, and Au-doped CdS (110) surfaces were determined and compared among them.

The atomic configurations of adsorbed $H_2S$ and $H_2O$ on the pristine CdS (110) surface and the nine different transition metal-doped surfaces are provided in Supplementary Table 3. Comparing the most stable configurations of $H_2S$, HS, $H_2O$, and OH, it is clear that the $H_2S$ molecule and single H atom are favorably absorbed and bound with one of the S atoms on the top layer in the pristine CdS and Cu, Zn, Ag, Au-doped CdS surfaces. However, in most of the HS adsorption systems, HS preferentially bonds with one TM atom. Conversely, in the $H_2O$ and OH adsorption systems, $H_2O$ and OH adsorbates tend to bond with TM atoms and two other adjacent Cd atoms to form a triangular conical structure.

The Gibbs free energy changes for $H_2S$, $H_2O$ and intermediates adsorbents were also calculated (Eq. (4) and Eq. (5)), since the adsorption of reactants and intermediates (e.g., chemisorption) on the catalyst surface is very relevant for a heterogeneous catalytic reaction, being the Gibbs free energy of OH, $\Delta G_{OH}$, normally considered as a descriptor for oxygen reduction reaction activity. Figure 6 shows the comparison of the calculated Gibbs free energy of $H_2O$ and $H_2S$ adsorption on the pristine CdS surface and the TM@CdS surfaces. A negative value of adsorption energy implies an exothermic chemisorption process. Within a suitable range of adsorption energies, the lower the adsorption energy, the higher the adsorption strength and capacity, which indicates stronger interaction between catalyst and adsorbate. As seen in Fig. 6, all studied systems, except Ni@CdS, present a negative value of the $H_2S$ adsorption energy. In addition, comparing the results with pristine CdS surface, after doping the surface with different transition metals, the adsorption energies for $H_2S$, HS, $H_2O$, and OH decrease, except for Au, Ni, Zn, and Cu @CdS surfaces.

As extracted from Fig. 6a, the Ni-doped surfaces require external energy for the $H_2S$ adsorption process, and the Au-doped surface releases less energy than pristine CdS surface for $H_2S$ adsorption process, indicating that Ni and Au dopants are not suitable for $H_2S$ splitting applications. In addition, it is observed in Fig. 6b that the $H_2O$ adsorption energy of Zn and Cu @CdS are less negative compared to pristine CdS surface, signifying relatively lower efficiency for $H_2O$ splitting applications. Conversely, the Ru, Rh, Pt doped CdS catalysts present very negative adsorption energies for all $H_2S$, HS, $H_2O$, and OH adsorption on the surface.

Since the Gibbs free energy of the elementary step of HER depends on the Gibbs free energy of intermediate H adsorption ($\Delta G_H$, see Eq. (6)), we have analyzed the adsorption characteristics of H on the Ni, Cu, Ru, Rh, Pd, Ag, Ir, Pt, and Au-doped CdS (110) surfaces. For this purpose, we have applied the Volmer–Heyrovský mechanism for the HER, which involves the adsorption of a proton following the electron deduction ($H^+ + e^-$) and the formation of H*, then in the next step generating molecular hydrogen ($\frac{1}{2}H_2$). Figure 7 presents the Gibbs free energy change of the pristine CdS surface and TM@CdS surfaces for HER. It shows that the $|\Delta G_H|$ for pristine CdS (1.11 eV) is very high compared to the results of TM-doped surfaces, indicating that the pristine CdS (110) surface is not highly efficient for the HER. Remarkably, Pt@CdS (0.18 eV), Rh@CdS (0.13 eV) and Pd@CdS (0.11 eV) surfaces show minimum values of $|\Delta G_H|$, demonstrating that these are the most active catalysts among all TM@ CdS surfaces for HER, in agreement with some experimental studies[22,46–48]. Meanwhile, Ag and Au @CdS systems show relatively lower HER activities with quite large values of $|\Delta G_H|$ (values of −0.82 and 1.05 eV, respectively).

Moreover, as shown in Supplementary Table 3, the structure of TM@CdS surfaces with H* adsorption demonstrates that H* prefers to be adsorbed at the top site of TM atoms, and there is a strong interaction between the H* atom and *d* orbitals of TM atoms, indicating that these metals act as active sites for HER. Considering that Cu, Au, Ni, and Zn-doped surfaces are not suitable for either

$H_2S$ or $H_2O$ splitting reactions, we selected six types of transition metals (Co, Ru, Rh, Pd, Ag, and Pt) for further investigating dual co-catalyst doped on CdS surface. Note that Zn-doped surfaces are discarded because they provide similar Gibbs adsorption energy values to bare CdS (see Figs. 6 and 7), not justifying the doping.

To further gain insights into the electron transfer and atomic interaction between the adsorbed H and the TM@CdS surfaces, we present in Fig. 8 the calculated charge density difference distributions (CDDD) for the pristine CdS and the selected six types of TM@CdS surfaces with H adsorption, calculated by Eq. (7). It is shown that the H atom interaction with the S atom in the pristine CdS surface leads to a charge rearrangement around the S and Cd atoms on the first and second layer of the material. In the pristine CdS system, there is a charge density reduction around the H atom and then the S atoms on the surface accept the corresponding electrons. When H adsorbs on the TM@CdS surface, the active sites shift to TM atoms and the charge distribution around TM atoms declines. Electrons are found to transfer from the adsorbed H atom to the first layer TM atoms, and TM@CdS surfaces are considerably polarized upon the adsorption of H, with the electrostatic interactions playing a key role. The polarization in the Rh@CdS, Pd@CdS and Pt@CdS systems are stronger with a larger CDDD isosurface and more charge transfer between H atom and surfaces than the other TM@CdS surfaces, giving rise to a larger interaction energy, which explains why Rh, Pd, and Pt co-catalysts give relatively higher reaction activity.

The partial density of states (PDOS) of the pristine CdS and the optimal TM@CdS surfaces are provided in Supplementary Fig. 2. For the PDOS of H adsorbed on pristine CdS, the spin-up and -down of density of states (DOS) are highly symmetric indicating that pristine CdS is a non-magnetic surface. In the DOS diagrams, the peaks between −6 and −2 eV are mostly contributed from *p* orbitals of sulfur, which is similar with TM@CdS systems. However, there are only small resonant peaks of H around 3 eV in the PDOS diagram of pristine CdS, in sharp contrast to the TM-doped systems. According to PDOS of TM@CdS, the *s* orbital of H always overlaps with the *d* orbital of the TM atoms, indicating a strong interaction between the H atom and TM atoms. The resonant peak of the *d* bands of TM atoms splits into several peaks in the energy range of −5 eV to 1 eV, and the hybridization peaks move to the lower energy range, especially for Co, Ru, Rh, and Pd atoms, resulting in a strong hybridization between TM and sulfur atoms in CdS surfaces.

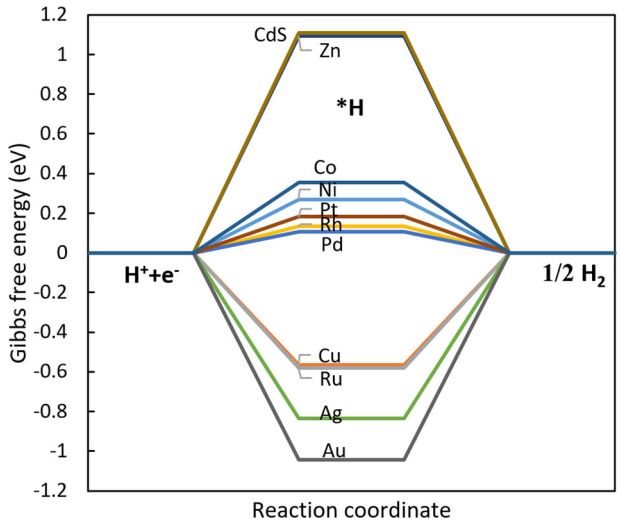


**Fig. 7 Gibbs free energy diagrams of the pristine CdS surface and TM@CdS surfaces for HER.** H* indicates the adsorbed hydrogen atom on the doped CdS surface. Data are available in Zenodo.

## High-throughput screening of TM1-TM2@CdS surfaces

According to previous experimental studies[13,22], dual co-decorated CdS photocatalysts have better efficiency for hydrogen generation under visible light irradiation. To select the optimal dual metal-doped CdS catalyst for HER applications, we have calculated the formation energies and the electronic structures of 21 TM1-TM2@CdS surfaces, as well as the Gibbs free energies of H adsorption on the surfaces. Supplementary Fig. 1c and d, show the geometry of the studied TM1-TM2@CdS (110) surfaces, where TM1 and TM2 denote the selected transition metals (i.e., Co, Ru, Rh, Pd, Ag and Pt) based on the analysis from previous sections. Similar to single-atom doped systems, TM1 and TM2 atoms have replaced two Cd atoms on the top layer of the surface. As shown in Fig. 9a, all the studied TM1-TM2@CdS surfaces present a negative formation energy ranging from −0.588 eV to −0.521 eV, indicating that these surfaces are thermodynamically stable. According to the colors of the heat map for the calculated formation energies, the Pd-Pd@CdS system shows the lowest formation energy (−0.588 eV) with the highest stability, and it is also more stable compared to the calculated formation energy of a single Pd atom doped system (−0.57 eV, as seen in Fig. 3). In addition, the formation energy of each TM1-TM2@CdS is different when compared to its corresponding single-doped system TM@CdS. Thus, the introduction of the second transition metal can change the stability of catalysts' samples.

As previously mentioned, the HER activity can be assessed by a crucial descriptor, i.e., the Gibbs free energy of hydrogen adsorption, $\Delta G_H$. We have calculated $\Delta G_H$ for the most stable configuration of H adsorption. The light green color in Fig. 9b

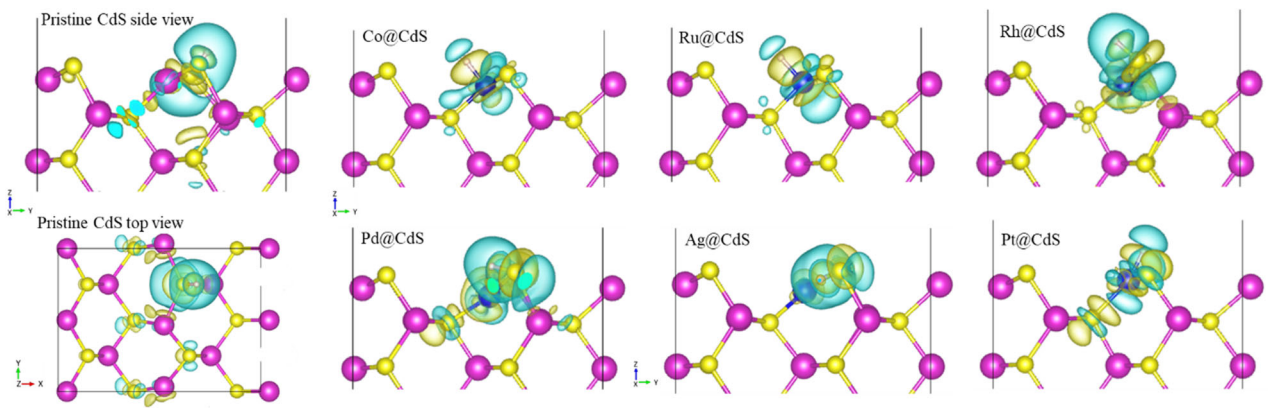


**Fig. 8 The charge density difference of the optimized H adsorption on the pristine CdS (110) surface and TM@CdS surfaces.** Same color code as Fig. 1, with H = white. Yellow (blue) isosurfaces represent electron accumulation (depletion) states.

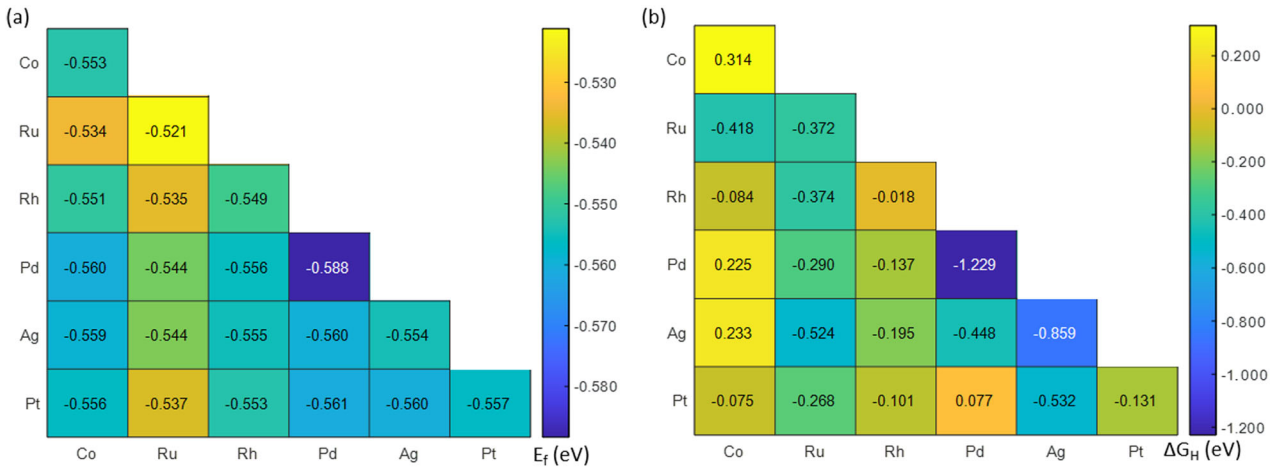


**Fig. 9 Formation energy (and Gibbs free energy of hydrogen adsorption for the studied 21TM1-TM2@CdS structures.** Formation energy, Ef (**a**), and Gibbs free energy, $\Delta G_H$ (**b**). The abscissa andordinate represent TM1 and TM2 of the TM1-TM2@CdS surfaces. The color responds to the value of the studied property for each surface, as indicated in the color scale. Data are available in Zenodo.

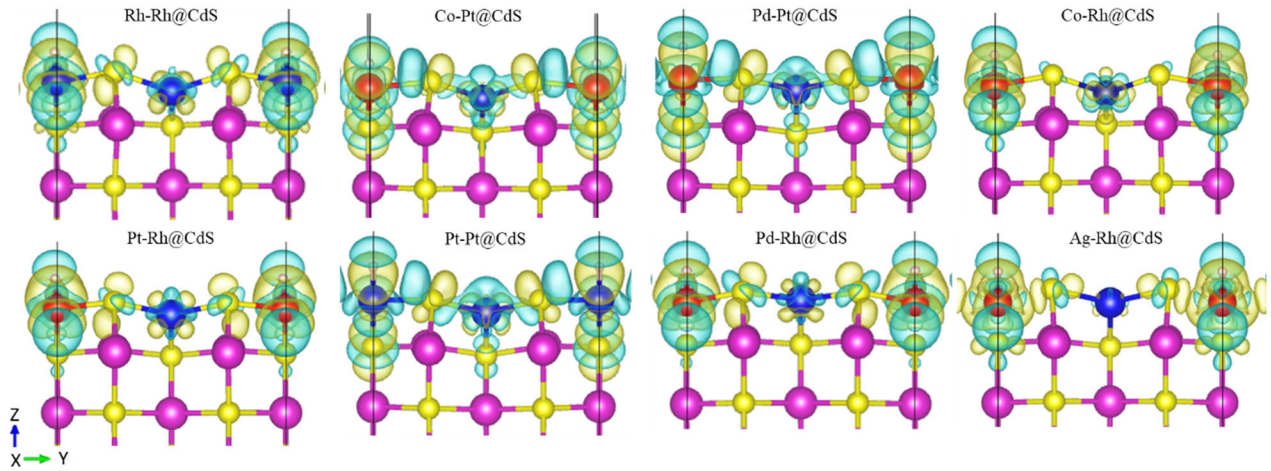


**Fig. 10 Charge density difference of the optimized H adsorption on the pristine CdS (110) surface and TM1-TM2@CdS surfaces.** Color code TM1 = blue, TM2 = red, the rest as Fig. 8. The order of dopants is the HER activity.

indicates $\Delta G_H$ values close to zero; the closer the value of $|\Delta G_H|$ to zero, the higher the HER activity is. Therefore, results indicate that Rh-Rh, Co-Pt, Pd-Pt, Co-Rh, Rh-Pt, Pt-Pt, Rh-Pd, and Rh-Ag@CdS have the potential to be excellent HER catalyst according to their small Gibbs free energies of hydrogen adsorption (−0.018, −0.075, 0.077, −0.084, −0.101, −0.131, −0.137, and −0.195 eV, respectively).

The CDDD of H adsorbed on these optimal TM1-TM2@CdS surfaces are shown in Fig. 10 to reveal the charge migration on the top layer of the surfaces. When the H atom bonds with TM2 atoms, a built-in electric field would form at the top layer of surface, which drives the electrons to migrate through dual metals, eventually reaching a new charge equilibrium. Strikingly, the electrons on the TM2 are transferred to the TM1, corroborating the strong electron coupling effect between the H, TM1, TM2 and sulfur atoms on the top layer. Compared with the CDDD of TM@CdS systems (see Fig. 8), doping dual metals on the surface can further facilitate the photogenerated electron transfer and greatly enhance the separation of the photogenerated electrons and hole.

The PDOS with the contribution from H and TMs atoms have been calculated to address the underlying mechanism of the H adsorption at the dual metal side. The plots are shown in Supplementary Fig. 3, revealing that there are large resonant peaks of H around 2 eV and −5 eV, and hybridized with the *d* orbitals of TM1 or TM2, exposing that the interaction between H orbitals and TM-d orbitals have been improved with the favorable synergetic effect of the presence of TM1 and TM2. The impurity states are completely occupied by doped TM atoms. More importantly, the electrons from a single TM atom can be shared and interact with another TM atom, creating new electronic states and new active sites. Thus, dual metal deposited on CdS can create and enlarge the reaction areas and serve as oxidation sites to consume the aggregated holes. Consequently, the propitious synergistic effects of TM1 and TM2 on electron extraction and hole depletion ensure an effective charge separation, resulting in a significant enhancement of the HER activity of the TM1-TM2@CdS photocatalysts.

Finally, to ensure the screened catalysts can be properly used for phocatalytic $H_2S$ and $H_2O$ splitting, the band structure of optimal TM1-TM2@CdS has been analyzed. Based on the results of the calculated band gap, CBM and VBM (see Supplementary Fig. 4), Rh-Rh@CdS presents a narrow band gap of 0.85 eV and insufficient negative CBM for the $H_2$ evolution potential, being removed in this later stage of the screening as a potential candidate of dual metal-doped CdS. Hence, loading dual co-catalyst including Pd-Pt, Rh-Pt, Pt-Pt and Rh-Pd@CdS show cooperative effects, providing a great potential to be used as ideal HER catalysts just for $H_2S$ splitting, while Co-Pt, Co-Rh, Rh-Ag

@CdS, with a small value of $\Delta G_H$ less than 0.2 eV and good stability, can be regarded as the most ideal HER catalysts for both $H_2S$ and water splitting.

In summary, a series of TM atoms embedded in the single Cd vacancy and dual Cd vacancies of the CdS (110) surface were systematically investigated to screen out the best materials for high-efficient HER. The screening and selection was performed based on key performance indicator descriptors, starting from their stability, band gap and *d*-band center, and activity. It was found that all the studied TM@CdS surfaces, except the Os@CdS, are stable, with uniformly embedded TMs into the CdS surface as active sites. Meanwhile, Cu, Rh, Pt, Pd, Ag, Au, Ni, Ru, Co, Zn @ CdS show suitable electronic properties for photocatalytic $H_2S$ splitting and $H_2O$ splitting. For the HER, six types of transition metals (Co, Ru, Rh, Pd, Ag, and Pt) doped on the surface show a lower $\Delta G_{adsorbate}$ (i.e., $H_2S$, HS, $H_2O$, OH, H) compared to pristine CdS surface, making them clear candidates for further investigation of dual co-catalysts doped on the CdS surface. Compared with the existing experimental work, this study predicts that a new type of catalyst (i.e., Co@CdS), not experimentally explored yet, could have good performance in $H_2S$ and $H_2O$ photocatalysis. Moreover, based on the calculated results for 21 co-doped TM1-TM2@CdS surfaces, the Co-Pt, Co-Rh and Rh-Ag@CdS structures show good stability and better HER activity for both $H_2S$ and water splitting applications than TM@CdS, suggesting the synthesis and experimental testing of these four novel photocatalysts.

The insights obtained from this work explain at the electronic and mechanistic levels why transition metals doped on CdS photocatalysts can improve the HER performance compared to the pristine CdS surface, with DFT allowing to quantify and rank the performance of the different doped surfaces. In addition, it has also been demonstrated that dual metal decorated CdS photocatalysts could dramatically improve the efficiency for HER compared to single metal decorated catalysts, which also provides robust guidance on synergy modulation for designing optimal catalyst candidates based on CdS for green hydrogen production.

## METHODS

### Computational details

Spin-polarized DFT calculations were performed with the VASP suite of programs (v6.2.0)[49]. The electron exchange-correlation interactions were described with the generalized gradient approximation (GGA) with the Perdew−Burke−Ernzerof (PBE)[50] functional, using the potentials supplied by VASP with the projector-augmented-wave (PAW) pseudopotentials[51]. Moreover, in order to accurately investigate the electronic structures of magnetic surfaces and avoid the underestimation of band gaps by PBE methods, we performed spin-polarized hybrid DFT calculations by using the Heyd-Scuseria-Ernzerhof (HSE06)[52] hybrid functional with a 25% Hartree–Fock exchange. The empirical correction (DFT-D3) was included to describe the long-range van der Waals (vdW) interactions. A plane-wave basis set with an energy cutoff of 500 eV was adopted in all calculations. The electronic self-consistency was converged to within $10^{-5}$ eV atom^-1, while the ionic positions were fully relaxed until the residual force acting on each ion was less than 0.02 eV Å^-1. Since the equilibrium morphology of CdS zinc-blended crystalline phase only consists of the (110) surface[53], we systematically studied the dopant of TMs on the CdS (110) surface by replacing one or two Cd atoms with TMs at the top layer of the surface. The bulk of $1 \times 1 \times 1$ unit cell, and slabs of $2 \times 2$ unit cells with seven layers were used. The upper three layers were allowed to relax while the bottom layers were constrained with bulk geometric parameters to simulate a bulk environment. Monkhorst–Pack *k*-point meshes of $4 \times 4 \times 4$ and $2 \times 3 \times 1$ were used for the CdS bulk system and for the slab systems, respectively. A full relaxation was performed searching for the optimal spin magnetization and to obtain the magnetic ground state, i.e., the minimum energy of the system. The spin magnetization of the doped TM systems was then calculated, after convergence, as: # electrons in the up-spin components - # of electrons in the down-spin components. It should be mentioned that, if the system corresponds to an isolated molecule/cluster, then the total magnetization will be an integer (etc. 0, 1, 2…). However, if for instance, the system is periodic (as in our case), the spin multiplicity is defined for the total system, not for the unit cell, and then decimal numbers may be obtained. Moreover, please notice that the spin-states of TM doping on the support can be different depending on whether it interacts with a pure or impurity site and may affect the reactivity of metal atoms. For a detailed explanation, the reader is referred to the work by Shalabi et al.[54]. To ensure the accuracy of the computational results, we first compared the parameters of the bulk system with experimental studies. The obtained optimized lattice parameters for bulk CdS (5.87 Å) and the band gap for CdS (110) surface (2.45 eV), are both in good agreement with the experimental values[55] and previous theoretical calculations[56].

### Energy calculations

The binding energy $(E_b)$ of the TM atoms embedded in the defective CdS surface was calculated as follows[39]:

$$E_b = E_{TM@CdS} - E_{CdS} - n.E_{TM} \quad (1)$$

where $n$ is the number of metal atoms in its bulk structure, $E_{TM@CdS}, E_{CdS}$ and $E_{TM}$ denote the total energies of TM-embedded CdS surface, defective CdS surface and TM atoms, respectively. A more negative $E_b$ value of TM atoms to the substrates indicates a better stability of the structure. Conversely, a more positive $E_b$ value of TM atoms denotes a higher possibility of TM agglomeration to form metal clusters on the catalyst surface, which could compromise the formation of active sites and the catalytic efficiency.

The cohesive energies of bulk metal materials $(E_c)$ can be obtained by[39]:

$$E_c = (E_{bulk} - n.E_{TM})/n \quad (2)$$

where the $E_{bulk}$ is the energy of bulk metal and $E_{TM}$ is the energy of a single metal atom.

In addition, the formation energy[57] of TM embedded in the defective CdS $(E_f)$ was calculated as:

$$E_f = (E_{TM@CdS} - a.\mu_{Cd} - b.\mu_S - n.\mu_{TM})/(a + b + n) \quad (3)$$

where $E_{TM@CdS}$ is the same as in Eq. (1), $a$ and $b$ are the number of Cd and S atoms in the system, respectively, and $\mu_{Cd}, \mu_S$and $\mu_{TM}$ are the chemical potentials of Cd, S, and TM from their bulk structure, respectively. A negative $E_f$ denotes that the synthesis process is exothermic and thermodynamically favorable.

The reaction activity was evaluated by calculating the Gibbs free energy for adsorbates as:

$$\Delta G_{adsorbate} = (\Delta E_{adsorbate} + \Delta E_{ZPE}) - T\Delta S \quad (4)$$

where $\Delta E_{adsorbate}$ represents the adsorption energy of molecules and intermediates ($H_2S$, HS, $H_2O$, OH and H), $T$ denotes the temperature 300 K, and $\Delta E_{ZPE}$ and $\Delta S$ are the difference in zero-point energy (ZPE) and the entropy between the adsorbed state and gas phase, respectively. Specifically, $\Delta E_{adsorbate}$ for $H_2S$, HS, $H_2O$, OH adsorbates were calculated as[35]:

$$\Delta E_{adsorbate} = E_{TM@CdS+adsorbate} - E_{TM@CdS} - E_{adsorbate} \quad (5)$$

where $E_{TM@CdS+adsorbate}$ denotes the energy of TM@CdS with $H_2S$, HS, $H_2O$ or OH adsorbates, and the $E_{adsorbate}$ is the energy of $H_2S$, HS, $H_2O$ and OH in the gas phase. Notably, the adsorption energy of H adsorbate was defined as[58]:

$$\Delta E_H = E_{TM@CdS+H} - E_{TM@CdS} - (1/2)E_{H_2} \quad (6)$$

where $E_{TM@CdS+H}$ represents the energy of TM@CdS with H* adsorbed hydrogen atoms, and the $E_{H_2}$ is the energy of $H_2$ in the gas phase. The BEP relation[59,60] and the Sabatier principle[61] has been extensively applied in the literature[62–67] for metal doping systems. Based on the BEP relation, the Sabatier principle states that the active site with a $\Delta G_H$ closest to zero (lower$|\Delta G_H|$) demonstrates the best $H_2$ evolution performance in electrocatalysis applications. A higher positive value of $\Delta G_H$ indicates a stronger resistance for the chemical reduction reaction; conversely, a more negative value of $\Delta G_H$ denotes that detaching protons from the catalyst surface will become more difficult[57]. Lopato and coworkers[68] reported that the Sabatier principle was also applicable to the photocatalytic $H_2$ evolution.

The charge density difference of the system, $\Delta\rho$, was calculated from[69]:

$$\Delta\rho = \rho_{TM@CdS+adsorbate} - \rho_{TM@CdS} - \rho_{adsorbate} \quad (7)$$

being $\rho_{TM@CdS+adsorbate}, \rho_{TM@CdS}$ *and* $\rho_{adsorbate}$ the charge density of TM@CdS surface with the adsorbate, surface and free adsorbate systems, respectively.

Simple but thermochemical reasonable descriptors enabling the representation of catalyst properties and photocatalytic activities are essential for discovering or designing new catalysts via computational screening. For instance, the formation energy of transition metal doping[36,37,39], band gap energy of catalysts[13,40], the *d*-band center for transition metals[43,70], and the gas adsorption energy of key reaction intermediates[41,58,69,71] have been commonly proposed to guide the screening protocol of catalysts in the literature. Figure 1 shows a schematic diagram of the followed screening process for determining the proper transition metals doped on the CdS (110) surface. The detailed process includes: (1) examination of the structural stability of different TM@CdS surfaces by calculating their corresponding binding energies ($E_b$), cohesive energies ($E_c$), and formation energies ($E_f$); (2) the band gap and *d*-band center were introduced as the second descriptor to estimate the optical and electronic properties, which can provide a basis for screening potential candidates for photocatalytic $H_2O$ and $H_2S$ splitting. For initiating the redox reaction of $H_2S$ and $H_2O$ splitting, the valence band edge potential (maximum valence band, VBM) should be more positive than the $S^{2-}$ oxidation level (0.14 V vs NHE at pH = 0) and water oxidation level (1.23 V vs NHE at pH = 0), respectively. While the edge potential of the conduction band (minimum conduction band, CBM) for both cases should be more negative than the $H_2$ evolution potential (0 V vs. NHE)[8]. In addition, the band gap width of semiconductors should be less than 3.0 eV (>400 nm) and greater than 1.23 eV (<1000 nm) to be utilized in the UV/visible region (i.e., wavelengths from ca. 380 to 750 nanometers). (3) The change in the Gibbs free energy of the adsorbed adsorbates $(\Delta G_{H2S}, \Delta G_{HS}, \Delta G_{H2O}, \Delta G_{OH}, \Delta G_H)$ was compared with pristine CdS surface to evaluate the HER activity.

## DATA AVAILABILITY

Data are available in the Zenodo open repository at https://doi.org/10.5281/zenodo.7056972.

Received: 26 June 2022; Accepted: 23 October 2022;
Published online: 10 November 2022

## REFERENCES

1. Wang, Q. et al. Scalable water splitting on particulate photocatalyst sheets with a solar-to-hydrogen energy conversion efficiency exceeding 1%. *Nat. Mater.* **15**, 611–615 (2016).
2. Oladipo, H., Yusuf, A., Al Jitan, S. & Palmisano, G. Overview and challenges of the photolytic and photocatalytic splitting of $H_2S$. *Catal. Today* **380**, 125–137 (2021).
3. Glenk, G. & Reichelstein, S. Economics of converting renewable power to hydrogen. *Nat. Energy* **4**, 216–222 (2019).
4. Kumaravel, V., Mathew, S., Bartlett, J. & Pillai, S. C. Photocatalytic hydrogen production using metal doped $TiO_2$: a review of recent advances. *Appl. Catal. B Environ.* **244**, 1021–1064 (2019).
5. Ahmad, H., Kamarudin, S. K., Minggu, L. J. & Kassim, M. Hydrogen from photocatalytic water splitting process: a review. *Renew. Sustain. Energy Rev.* **43**, 599–610 (2015).
6. Dan, M. et al. Hydrogen sulfide conversion: How to capture hydrogen and sulfur by photocatalysis. *J. Photochem. Photobiol. C. Photochem. Rev.* **42**, 100339 (2020).
7. De Crisci, A. G., Moniri, A. & Xu, Y. Hydrogen from hydrogen sulfide: towards a more sustainable hydrogen economy. *Int. J. Hydrog. Energy* **44**, 1299–1327 (2019).
8. Li, Y., Bahamon, D., Sinnokrot, M. & Vega, L. F. Computational modeling of green hydrogen generation from photocatalytic $H_2S$ splitting: Overview and perspectives. *J. Photochem. Photobiol. C. Photochem. Rev.* **49**, 100456 (2021).
9. Harb, M. & Cavallo, L. Toward the design of new suitable materials for solar water splitting using density functional theory. *ACS Omega* **3**, 18117–18123 (2018).
10. Kudo, A. & Miseki, Y. Heterogeneous photocatalyst materials for water splitting. *Chem. Soc. Rev.* **38**, 253–278 (2009).
11. Nasir, J. A. et al. Recent developments and perspectives in CdS-based photocatalysts for water splitting. *J. Mater. Chem. A* **8**, 20752–20780 (2020).
12. Cheng, L., Xiang, Q., Liao, Y. & Zhang, H. CdS-Based photocatalysts. *Energy Environ. Sci.* **11**, 1362–1391 (2018).
13. Wei, R. et al. Dual-cocatalysts decorated rimous CdS spheres advancing highly-efficient visible-light photocatalytic hydrogen production. *Appl. Catal. B Environ.* **231**, 101–107 (2018).
14. Jin, J., Yu, J., Liu, G. & Wong, P. K. Single crystal CdS nanowires with high visible-light photocatalytic $H_2$ production performance. *J. Mater. Chem. A* **1**, 10927–10934 (2013).
15. Zhang, L. et al. Ultra-low content of Pt modified CdS nanorods: one-pot synthesis and high photocatalytic activity for $H_2$ production under visible light. *J. Mater. Chem. A* **3**, 23732–23742 (2015).
16. Yang, F. et al. Embedding Pt nanoparticles at the interface of CdS/$NaNbO_3$ nanorods heterojunction with bridge design for superior Z-Scheme photocatalytic hydrogen evolution. *Appl. Catal. B Environ.* **278**, 119290 (2020).
17. Berr, M. et al. Colloidal CdS nanorods decorated with subnanometer sized Pt clusters for photocatalytic hydrogen generation. *Appl. Phys. Lett.* **97**, 93108 (2010).
18. Bao, N., Shen, L., Takata, T. & Domen, K. Self-templated synthesis of nanoporous CdS nanostructures for highly efficient photocatalytic hydrogen production under visible light. *Chem. Mater.* **20**, 110–117 (2008).
19. Darwent, J. R. & Porter, G. Photochemical hydrogen production using cadmium sulphide suspensions in aerated water. *J. Chem. Soc. Chem. Commun.* **4**, 145–146 (1981).
20. Sathish, M., Viswanathan, B. & Viswanath, R. P. Alternate synthetic strategy for the preparation of CdS nanoparticles and its exploitation for water splitting. *Int. J. Hydrog. Energy* **31**, 891–898 (2006).
21. Sathish, M. & Viswanath, R. P. Photocatalytic generation of hydrogen over mesoporous CdS nanoparticle: Effect of particle size, noble metal and support. *Catal. Today* **129**, 421–427 (2007).
22. Ma, G. et al. Direct splitting of $H_2S$ into $H_2$ and S on CdS-based photocatalyst under visible light irradiation. *J. Catal.* **260**, 134–140 (2008).
23. Wang, Y., Wang, Y. & Xu, R. Photochemical deposition of Pt on CdS for $H_2$ evolution from water: markedly enhanced activity by controlling Pt reduction environment. *J. Phys. Chem. C.* **117**, 783–790 (2013).
24. Darwent, J. R. $H_2$ production photosensitized by aqueous semiconductor dispersions. *J. Chem. Soc. Faraday Trans. 2 Mol. Chem. Phys.* **77**, 1703–1709 (1981).
25. Su, J., Zhang, T., Li, Y., Chen, Y. & Liu, M. Photocatalytic activities of copper doped cadmium sulfide microspheres prepared by a facile ultrasonic spray-pyrolysis method. *Molecules* **21**, 735 (2016).
26. Simon, T. et al. Redox shuttle mechanism enhances photocatalytic $H_2$ generation on ni-decorated CdS nanorods. *Nat. Mater.* **13**, 1013–1018 (2014).
27. Yan, H. et al. Visible-light-driven hydrogen production with extremely high quantum efficiency on Pt-PdS/CdS photocatalyst. *J. Catal.* **266**, 165–168 (2009).
28. Pareek, A., Thotakuri, R., Dom, R., Kim, H. G. & Borse, P. H. Nanostructure Zn–Cu co-doped CdS chalcogenide electrodes for opto-electric-power and $H_2$ generation. *Int. J. Hydrog. Energy* **42**, 125–132 (2017).
29. Yu, H., Huang, X., Wang, P. & Yu, J. Enhanced photoinduced-stability and photocatalytic activity of CdS by dual amorphous cocatalysts: synergistic effect of Ti(IV)-hole cocatalyst and Ni(II)-electron cocatalyst. *J. Phys. Chem. C.* **120**, 3722–3730 (2016).
30. Yang, J., Wang, D., Han, H. & Li, C. Roles of cocatalysts in photocatalysis and photoelectrocatalysis. *Acc. Chem. Res.* **46**, 1900–1909 (2013).
31. Nandy, A. et al. Computational discovery of transition-metal complexes: from high-throughput screening to machine learning. *Chem. Rev.* **121**, 9927–10000 (2021).
32. Borboudakis, G. et al. Chemically intuited, large-scale screening of MOFs by machine learning techniques. *npj Comput. Mater.* **3**, 40 (2017).

33. Kumar, R. & Singh, A. K. Chemical hardness-driven interpretable machine learning approach for rapid search of photocatalysts. *npj Comput. Mater.* **7**, 197 (2021).
34. Nørskov, J. K., Bligaard, T., Rossmeisl, J. & Christensen, C. H. Towards the computational design of solid catalysts. *Nat. Chem.* **1**, 37–46 (2009).
35. Zhou, Z., Han, F., Guo, L. & Prezhdo, O. V. Understanding divergent behaviors in the photocatalytic hydrogen evolution reaction on CdS and ZnS: A DFT based study. *Phys. Chem. Chem. Phys.* **18**, 16862–16869 (2016).
36. Garg, P., Nair, A. S., Rawat, K. S. & Pathak, B. Computational screening of electrocatalytic activity of transition metal-doped CdS nanotubes for water splitting. *J. Phys. Chem. C.* **123**, 13419–13427 (2019).
37. Wu, J. C., Zheng, J., Wu, P. & Xu, R. Study of native defects and transition-metal (Mn, Fe, Co, and Ni) doping in a zinc-blende CdS photocatalyst by DFT and hybrid DFT calculations. *J. Phys. Chem. C.* **115**, 5675–5682 (2011).
38. Kim, H. J., Lee, G., Jang, M. G., Noh, K. J. & Han, J. W. Rational design of transition metal co-doped ceria catalysts for low-temperature CO oxidation. *ChemCatChem* **11**, 2288–2296 (2019).
39. Lu, S., Huynh, H. L., Lou, F., Guo, K. & Yu, Z. Single transition metal atom embedded antimonene monolayers as efficient trifunctional electrocatalysts for the HER, OER and ORR: a density functional theory study. *Nanoscale* **13**, 12885–12895 (2021).
40. Wei, S., Wang, F., Dan, M., Yu, S. & Zhou, Y. Vanadium (V) and Niobium (Nb) as the most promising co-catalysts for hydrogen sulfide splitting screened out from 3d and 4d transition metal single atoms. *Int. J. Hydrog. Energy* **45**, 17480–17492 (2020).
41. Wang, Y. et al. High-throughput screening of carbon-supported single metal atom catalysts for oxygen reduction reaction. *Nano Res.* **15**, 1054–1060 (2022).
42. Miller, S., Dsilva, C. & Kitchin, J. R. Coverage dependent adsorption properties of atomic adsorbates on late transition metal surfaces. *Catalysis* **24**, 83–115 (2012).
43. Takigawa, I., Shimizu, K. I., Tsuda, K. & Takakusagi, S. Machine-learning prediction of the d-band center for metals and bimetals. *RSC Adv.* **6**, 52587–52595 (2016).
44. Bhattacharjee, S., Waghmare, U. V. & Lee, S. C. An improved d-band model of the catalytic activity of magnetic transition metal surfaces. *Sci. Rep.* **6**, 35916 (2016).
45. Gao, G., Waclawik, E. R. & Du, A. Computational screening of two-dimensional coordination polymers as efficient catalysts for oxygen evolution and reduction reaction. *J. Catal.* **352**, 579–585 (2017).
46. Yang, J. et al. Roles of cocatalysts in Pt-PdS/CdS with exceptionally high quantum efficiency for photocatalytic hydrogen production. *J. Catal.* **290**, 151–157 (2012).
47. Chen, X. & Shangguan, W. Hydrogen production from water splitting on CdS-based photocatalysts using solar light. *Front. Energy* **7**, 111–118 (2013).
48. Yao, W., Song, X., Huang, C., Xu, Q. & Wu, Q. Enhancing solar hydrogen production via modified photochemical treatment of Pt/CdS photocatalyst. *Catal. Today* **199**, 42–47 (2013).
49. Kresse, G. & Furthmüller, J. Efficiency of ab-initio total energy calculations for metals and semiconductors using a plane-wave basis set. *Comput. Mater. Sci.* **6**, 15–50 (1996).
50. Hammer, B., Hansen, L. B. & Nørskov, J. K. Improved adsorption energetics within density-functional theory using revised Perdew-Burke-Ernzerhof functionals. *Phys. Rev. B - Condens. Matter Mater. Phys.* **59**, 7413–7421 (1999).
51. Joubert, D. From ultrasoft pseudopotentials to the projector augmented-wave method. *Phys. Rev. B - Condens. Matter Mater. Phys.* **59**, 1758–1775 (1999).
52. Heyd, J., Scuseria, G. E. & Ernzerhof, M. Hybrid functionals based on a screened Coulomb potential. *J. Chem. Phys.* **118**, 8207–8215 (2003).
53. Shah, S. H., Azam, A. & Rafiq, M. A. Atomistic simulations of CdS morphologies. *Cryst. Growth Des.* **15**, 1792–1800 (2015).
54. Shalabi, A. S., Assem, M. M. & Soliman, K. A. Adsorption and spin state properties of Cr, Ni, Mo, and Pt deposited on $Li^+$ and $Na^+$ monovalent cation impurities of MgO (001) surface: DFT calculations. *J. Mol. Model.* **17**, 3299–3308 (2011).
55. Crystallographic data on minerals. In *CRC Handbook of Chemistry and Physics* (ed. David, R. L.), 156–166 (CRC Press, Boca Raton, FL, 2005).
56. Liu, J. Origin of high photocatalytic efficiency in monolayer g-$C_3N_4$/CdS heterostructure: a hybrid DFT study. *J. Phys. Chem. C.* **119**, 28417–28423 (2015).
57. Kirklin, S. et al. The open quantum materials database (OQMD): assessing the accuracy of DFT formation energies. *npj Comput. Mater.* **1**, 15010 (2015).
58. Zeng, Z. et al. Computational screening study of double transition metal carbonitrides $M'_2M''CNO_2$-MXene as catalysts for hydrogen evolution reaction. *npj Comput. Mater.* **7**, 2–8 (2021).
59. Thompson, W. A., Sanchez Fernandez, E. & Maroto-Valer, M. M. Review and analysis of $CO_2$ photoreduction kinetics. *ACS Sustain. Chem. Eng.* **8**, 4677–4692 (2020).
60. Evans, M. G. & Polanyi, M. Inertia and driving force of chemical reactions. *Trans. Faraday Soc.* **34**, 11–24 (1938).
61. Laursen, A. B. et al. Electrochemical hydrogen evolution: Sabatiers principle and the volcano plot. *J. Chem. Educ.* **89**, 1595–1599 (2012).
62. Tian, L., Li, Z., Xu, X. & Zhang, C. Advances in noble metal (Ru, Rh, and Ir) doping for boosting water splitting electrocatalysis. *J. Mater. Chem. A.* **9**, 13459–70 (2021).
63. Zhou, Y. et al. Computational screening of transition-metal single atom doped $C_9N_4$ monolayers as efficient electrocatalysts for water splitting. *Nanoscale* **11**, 18169–18175 (2019).
64. Zhao, Z. et al. The strain and transition metal doping effects on monolayer $Cr_2O_3$ for hydrogen evolution reaction: the first principle calculations. *Int. J. Hydrog. Energy* **47**, 0360–3199 (2021).
65. Jain, A., Sadan, M. B. & Ramasubramaniam, A. Promoting active sites for hydrogen evolution in $MoSe_2$ via transition-metal doping. *J. Phys. Chem. C.* **124**, 12324–12336 (2020).
66. Jin, H. et al. Heteroatom-doped transition metal electrocatalysts for hydrogen evolution reaction. *ACS Energy Lett.* **4**, 805–810 (2019).
67. Partanen, L., Alberti, S. & Laasonen, K. Hydrogen adsorption trends on two metal-doped $Ni_2P$ surfaces for optimal catalyst design. *Phys. Chem. Chem. Phys.* **23**, 11538–47 (2021).
68. Lopato, E. M. et al. Parallelized screening of characterized and DFT-modeled bimetallic colloidal cocatalysts for photocatalytic hydrogen evolution. *ACS Catal.* **10**, 4244–4252 (2020).
69. Zhu, X. et al. Activity origin and design principles for oxygen reduction on dual-metal-site catalysts: a combined density functional theory and machine learning study. *J. Phys. Chem. Lett.* **10**, 7760–7766 (2019).
70. Yeo, B. C. et al. High-throughput computational-experimental screening protocol for the discovery of bimetallic catalysts. *npj Comput. Mater.* **7**, 1–10 (2021).
71. Mao, X. et al. Computational high-throughput screening of alloy nanoclusters for electrocatalytic hydrogen evolution. *npj Comput. Mater.* **7**, 46 (2021).

## ACKNOWLEDGEMENTS

We acknowledge the financial support of Khalifa University of Science and Technology, under project RC2-2019-007 (Research and Innovation Center on $CO_2$ and Hydrogen, RICH Center). Yuting Li acknowledges a grant from the China Scholarship Council (CSC), which has sponsored the author's PhD study at Khalifa University of Science and Technology. Computational resources from the RICH center and the Almesbar HPC at the Research Computing Department at Khalifa University are gratefully acknowledged.

## AUTHOR CONTRIBUTIONS

Y.L. performed the computational studies and drafted the manuscript. D.B. and M.S. assisted with the interpretation of the DFT results. L.V. assisted with the methodology, designed, and supervised the computational work. All authors contributed to the writing and final edition of the manuscript.

## COMPETING INTERESTS

The authors declare no competing interests.

## ADDITIONAL INFORMATION

**Supplementary information** The online version contains supplementary material available at https://doi.org/10.1038/s41524-022-00922-4.

**Correspondence** and requests for materials should be addressed to Lourdes F. Vega.

**Reprints and permission information** is available at http://www.nature.com/reprints

**Publisher's note** Springer Nature remains neutral with regard to jurisdictional claims in published maps and institutional affiliations.